

## Article

# Effects of Boride Orientation and Si Content on High-Temperature Oxidation Resistance of Directionally Solidified Fe–B Alloys

Pengjia Guo <sup>1</sup>, Shengqiang Ma <sup>1,\*</sup>, Xuebin He <sup>2</sup>, Ping Lv <sup>1</sup>, Yang Luo <sup>1</sup>, Junhong Jia <sup>3</sup>, Xudong Cui <sup>2</sup>, Liuji Xu <sup>4</sup> and Jiandong Xing <sup>1</sup>

<sup>1</sup> State Key Laboratory for Mechanical Behavior of Materials, School of Materials Science and Engineering, Xi'an Jiaotong University, Xi'an 710049, China

<sup>2</sup> Shaanxi Union Research Center of University and Enterprise for Zinc-Based New Materials, Xi'an 710049, China

<sup>3</sup> College of Mechanical & Engineering, Shaanxi University of Science and Technology, Xi'an 710021, China

<sup>4</sup> National Joint Engineering Research Center for Abrasion Control and Molding of Metal Materials, Henan University of Science and Technology, Luoyang 471000, China

\* Correspondence: sqma@mail.xjtu.edu.cn

**Abstract:** In this work, the as-cast directionally solidified (DS) Fe–B alloys with various Si contents and different boride orientation were designed and fabricated, and the as-cast microstructures and static oxidation behaviors of the DS Fe–B alloys were investigated extensively. The as-cast microstructure of the DS Fe–B alloys consists of the well-oriented Fe<sub>2</sub>B columnar grains and α-Fe, which are strongly refined by Si addition. The oxidation interface of the scales in the DS Fe–B alloy with 3.50 wt.% Si demonstrates an obvious saw-tooth shaped structure and is embedded into the alternating distributed columnar layer structures of the DS Fe–B alloy with oriented Fe<sub>2</sub>B and α-Fe matrix, which is beneficial to improve the anti-peeling performance of the oxide film compared with lower amounts of Si addition in DS Fe–B alloys with oriented Fe<sub>2</sub>B [002] orientation parallel to the oxidation direction (i.e., oxidation diffusion direction, labeled as Fe<sub>2</sub>B<sub>//</sub> sample). In the DS Fe–B alloys with oriented Fe<sub>2</sub>B [002] orientation vertical to the oxidation direction (i.e., labeled as Fe<sub>2</sub>B<sub>⊥</sub> sample), due to the blocking and barrier effect of laminated-structure boride, Si is mainly enriched in the lower part of the oxide film to form a dense SiO<sub>2</sub> thin layer adhered to layered boride. As a result, the internal SiO<sub>2</sub> thin layer plays an obstructed and shielded role in oxidation of the substrate, which hinders the further internal diffusion of oxygen ions and improves the anti-oxidation performance of the Fe<sub>2</sub>B<sub>⊥</sub> sample, making the average anti-oxidation performance better than that of the Fe<sub>2</sub>B<sub>//</sub> sample.

**Keywords:** directionally solidified (DS) Fe–B alloys; boride orientation; static oxidation; anti-oxidation performance



**Citation:** Guo, P.; Ma, S.; He, X.; Lv, P.; Luo, Y.; Jia, J.; Cui, X.; Xu, L.; Xing, J. Effects of Boride Orientation and Si Content on High-Temperature Oxidation Resistance of Directionally Solidified Fe–B Alloys. *Materials* **2022**, *15*, 7819. <https://doi.org/10.3390/ma15217819>

Academic Editor: Francesco Iacoviello

Received: 5 October 2022

Accepted: 3 November 2022

Published: 5 November 2022

**Publisher's Note:** MDPI stays neutral with regard to jurisdictional claims in published maps and institutional affiliations.



**Copyright:** © 2022 by the authors. Licensee MDPI, Basel, Switzerland. This article is an open access article distributed under the terms and conditions of the Creative Commons Attribution (CC BY) license (<https://creativecommons.org/licenses/by/4.0/>).

## 1. Introduction

In the past few decades, many efforts have been made to improve the high-temperature corrosion-wear behaviors of metal materials in metal liquids during the liquid metal forming [1–5]. There is good evidence that Fe–B alloys have good corrosion resistance due to the formation of a large number of stable and continuous borides in the matrix [6–10]. Moreover, boron has a very limited solubility in iron to consequently form borides, while carbon is almost insoluble in borides to produce carbides or largely dissolve into the iron matrix. Accordingly, the unique microstructures and properties of Fe–B alloys can be easily regulated by wide-range adjustment of the boron and carbon contents to control the hard-phase and anti-corrosive Fe<sub>2</sub>B and the continuously distributed metal matrix, which achieves independent control of the wear-resistant phase and matrix structure. Therefore,

this alloy has better hardenability, fracture toughness and wear resistance compared to other iron-based alloys and steels [11–17]. As the primary alloying element, the high-temperature corrosion behaviors of borides have been investigated widely. Yan et al. examine the high-temperature behavior of the boride layer of 45# carbon steel and found that no oxidation occurred before 730 °C and only slight oxidation of the boride layer between 730 and 930 °C [18]. Kim et al. have reported that the addition of boron can improve the cavitation erosion resistance of Fe-Based hard-facing alloys [19]. Furthermore, Klein and Wu et al. revealed that appropriate B content in Co- and Nb-based alloys leads to improved oxidation resistance and oxide layer adhesion [20,21]. It has been found that borides tend to be oxidized to form  $B_2O_3$  with a melting point of 450 °C at high temperatures [22].  $B_2O_3$  is highly hygroscopic and forms volatile  $HBO_2$  by forming B–O–H bonds with  $H_2O$  in the air [23,24]. In this case, the volatilization and fluidity of glassy state  $B_2O_3$  may generate some pores in the matrix, which allows the rapid diffusion of O ions, resulting in poor high-temperature oxidation resistance of Fe–B alloys. Pozdniakov et al. found that the steel with a high boron content was an important material for the production of spent nuclear fuel storage with little uncontrollable hot deformation behavior, in which the stainless-steel benefits from the distinct features of boron-containing steels [25].

Although some of the effects of boron content on high-temperature oxidation resistance of Fe–B alloys has been studied, the research on the high-temperature oxidation resistance of the DS Fe–B alloys by Si addition still lacks an understanding of the performance of oxidation. At present, the role of Si in high-speed steel has attracted more attention to discover its beneficial effects, such as formation of carbides, grain refinement and solid solution strengthening [26–29]. Moreover, Ju et al. investigated that Fe-10Cr-1.5B-6Al-0.3C-0.8Mn-0.6Si alloys reporting that they exhibited superior oxidation resistance at 900 °C [30]. Studies have also shown that the  $SiO_2$  layer generated at the interface of the oxide film can hinder ion diffusion [31]. Lv et al. reported that  $B_2O_3$ – $SiO_2$  oxides accumulate in the inner oxide layer during chemical friction under high-temperature conditions, which improved the oxidation behavior of Fe–B alloys [32]. However, the effect of Si content and boride orientation on the high-temperature oxidation resistance of DS Fe–B alloy still needs to be studied to uncover the underlying synergistic actions. In this work, as-cast DS Fe–B alloys with various Si contents and boride orientations were designed and fabricated, the as-cast microstructures and static oxidation behaviors were investigated extensively to illustrate the synergistic effect of Si and the orientation of borides in DS Fe–B alloy.

## 2. Materials and Methods

### 2.1. Sample Preparation

The chemical composition of the investigated Fe–B alloys containing Si is listed in Table 1. Four samples of the Fe–B alloy with different Si contents were prepared and denoted as A1, A2, A3, and A4 samples. The Fe–B alloys were melted in a 10 kg vacuum induction melting furnace with charged materials of pure iron, ferrosilicon and ferrochromium [33]. When all the charged materials were melted in the furnace, the pre-heated raw ferroboration was added into the furnace after being deoxidize with a small amount of pure aluminum. Once the alloy had melted at 1450–1480 °C, it was poured into the designed circulating water-cooled mold to solidify directional (DS) microstructures, i.e., obtaining Y-block ingots of the DS Fe–B alloy, as shown in Figure 1. The directional region near the chilled mold, where the sample with an average solidification rate of approximately 16 °C/s was measured by a thermocouple [34]. The oxidation samples were prepared for the oxidation direction parallel to the preferential growth direction of  $Fe_2B$  (i.e., defined as  $Fe_2B_{//}$  sample) and the oxidation direction perpendicular to the  $Fe_2B$  preferential growth direction (defined as  $Fe_2B_{\perp}$  sample). The DS samples with two oxidation manners, that is, the  $Fe_2B_{//}$  sample and the  $Fe_2B_{\perp}$  sample, were oxidized at an elevated temperature with the oxidation direction parallel to the  $Fe_2B$  [002] orientation and vertical to the  $Fe_2B$  [002] orientation, and positions of the oxidation samples were cut from the Y-shaped DS ingots with the dimensions of 15 mm × 10 mm × 3 mm, as schematically

shown in Figure 2. In order to prevent other surfaces of the sample from oxidation which may affect the experimental results, a small brush to apply an  $\text{Al}_2\text{O}_3$  coating was used to overlay the coating on to the non-oxidized side of the specimen.

**Table 1.** Chemical compositions of cast DS Fe–B alloy by spark emission spectrometer (wt.%).

Samples	B	Cr	Si	C	Fe
A1	3.51	0.52	0.00	0.11	Bal
A2	3.51	0.50	1.50	0.10	Bal
A3	3.49	0.50	2.50	0.12	Bal
A4	3.50	0.51	3.50	0.11	Bal

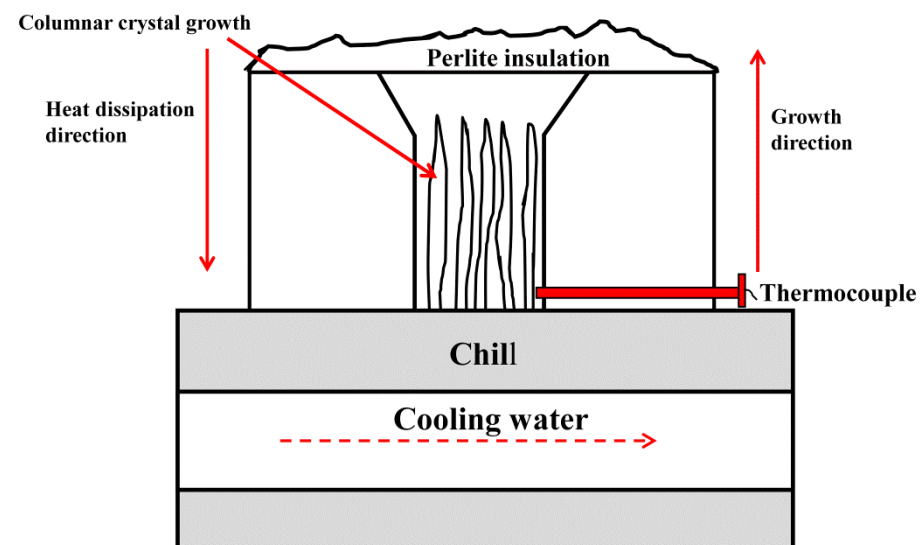


**Figure 1.** The schematic device of DS (directionally solidified) cast Fe–B alloy.

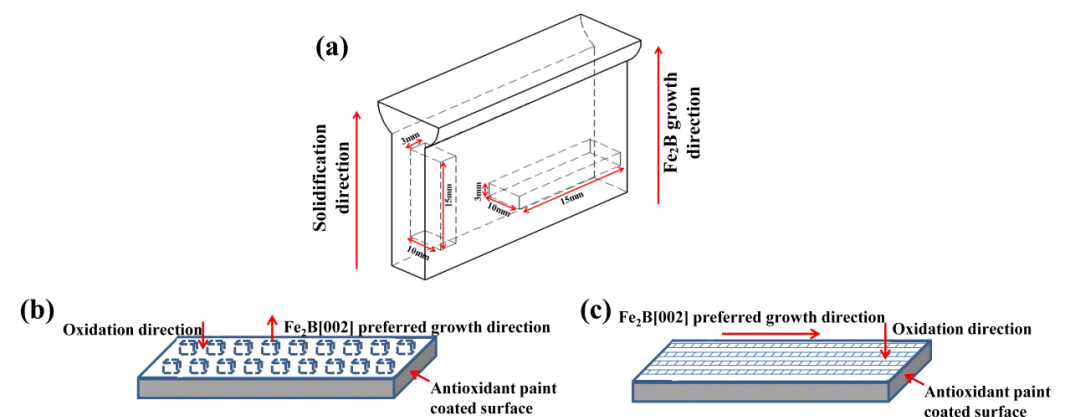


**Figure 2.** Schematic diagram of different oriented boride oxide samples: (a) Schematic diagram of sample position for high-temperature oxidation; (b)  $\text{Fe}_2\text{B}_{//}$  samples; (c)  $\text{Fe}_2\text{B}_{\perp}$  samples.

## 2.2. Static Oxidation

The static oxidation experiment method followed the Chinese national standards (GB/T 13303–91) [35]. The static oxidation tests were carried out in a box-type resistance furnace in air at 1073 K (with  $\pm 3$  K) for a total oxidation time of 100 h. [32]. The static oxidation test was maintained at 20 h, 40 h, 60 h, 80 h and 100 h. After the oxidation test, the samples were cooled down in the furnace and then the weight gains were measured at room temperature on an electronic balance with a precision of 0.01 mg. In order to ensure

the spalling of the scales, the samples were put into a crucible and the weight gains of the spalling scale after different oxidation durations were measured and calculated together according to GB/T 13303–91. Three repeated tests were conducted to obtain the average weight gain. The equipment used for static oxidation experiments is illustrated in Figure 3.

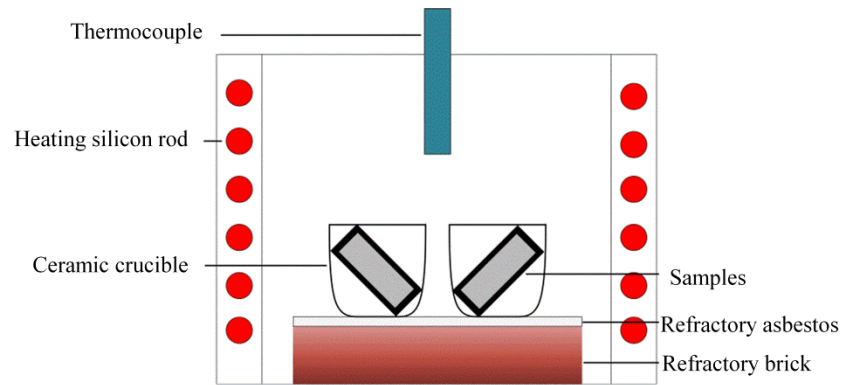


**Figure 3.** Schematic diagram of the static oxidation experiment apparatus.

### 2.3. Characterization

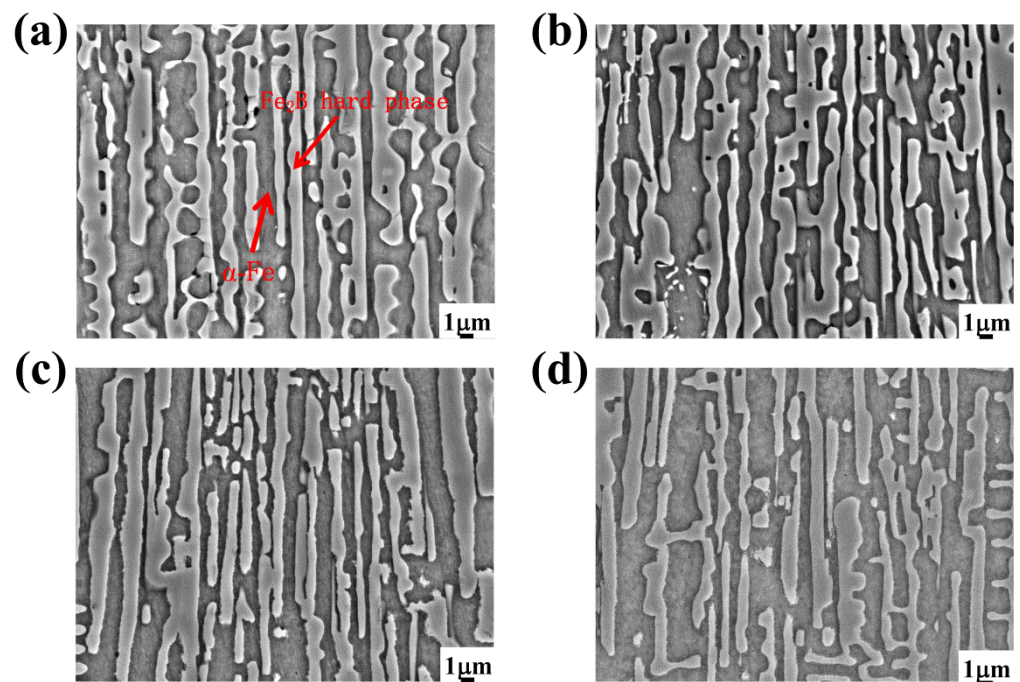
All the metallographic specimens were polished using a diamond polishing agent with diamond particles of 0.5  $\mu\text{m}$  suspended in a polishing fluid, and then etched using a 4%  $\text{HNO}_3$  solution. Samples with transverse sections of oxidation were prepared and planted with chemical nickel-plating, and then mounted in resin. After grinding with SiC sandpaper of up to 1500#, and polished by flannelette, the transverse sections of the oxidation samples were slightly etched using a 4%  $\text{HNO}_3$  solution. The microstructures of the as-cast samples were examined by scanning electron microscopy (SEM, VEGAII, XMUINCA, TESCAN, Brno, Czech Republic) and X-ray diffraction (XRD, D/Max-2400X, Rigaku Corporation, Tokyo, Japan). The MDI Jade 6 was used to identify (MDI Jade 6, Materials Data Management Inc., Indianapolis, IN, USA) the phase constituents of the as-cast and oxidation samples of the DS Fe–B alloys. The as-cast and cross-sectional samples before and after oxidation were characterized using X-ray diffraction (XRD), and scanning electron microscopy (SEM) with energy dispersive spectroscopy (EDS) to investigate the microstructures and morphologies as well as the scale thickness.

## 3. Results and Discussion

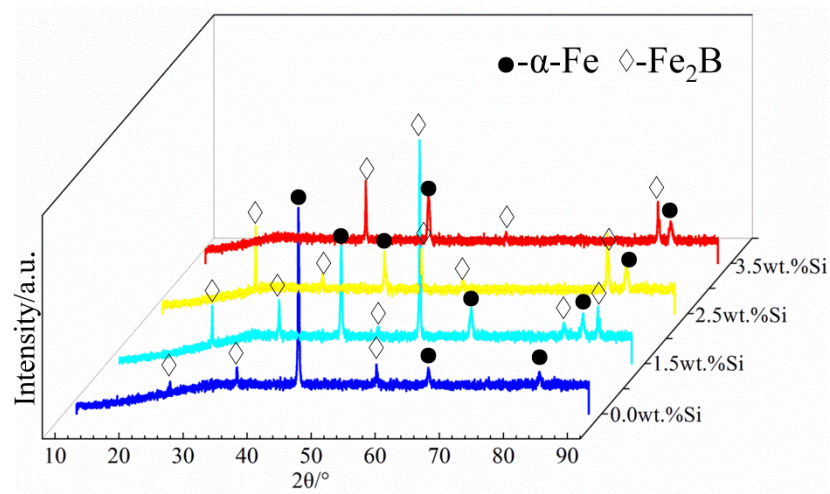
### 3.1. As-Cast Microstructure

Figure 4 shows the scanning electron microstructure images of the test alloys in the as-cast condition with different Si contents. From Figure 4, it can be seen that all the test alloys formed a metallic matrix and eutectic boride [36–38]. Clearly, the microstructures of the DS Fe–B alloys containing various Si addition showed good orientation effects. The columnar gray  $\text{Fe}_2\text{B}$  were arranged with long rods with a preferred growth orientation of columnar  $\text{Fe}_2\text{B}$  [002] crystal orientation [7,34]. Furthermore, the gray-white  $\alpha\text{-Fe}$  matrix was distributed among the lamellar structures of columnar  $\text{Fe}_2\text{B}$ , exhibiting dual-phase oriented microstructures of the DS Fe–B alloys (Figure 4). Additionally, the lamellar space of the columnar  $\text{Fe}_2\text{B}$  was greatly refined by Si addition. Figure 5 shows the XRD patterns of the as-cast DS Fe–B alloys with different Si contents. It can be seen that the as-cast microstructures of the longitudinal section of DS Fe–B alloy mainly comprised  $\text{Fe}_2\text{B}$  (36-1332) indexed with lots of strong peaks as well as the presence of some  $\alpha\text{-Fe}$  peaks (06-0696) [32,39]. Obviously, the increasing Si addition resulted in the vanishing peaks of some small diffraction angles and strengthened peaks of large diffraction angles for oriented  $\text{Fe}_2\text{B}$ , which may be influenced by the various oriented crystal planes of  $\text{Fe}_2\text{B}$  grain in its lateral grain plane (i.e., prismatic plane of  $\text{Fe}_2\text{B}$  with strong faceted crystal growth). Meanwhile, with the increase in Si content, there was no new phase in the DS Fe–B alloys,

which indicates that Si just dissolves into the matrix and refines the lamellar structures of  $\alpha$ -Fe and  $\text{Fe}_2\text{B}$  [34].



**Figure 4.** SEM micrographs of the as-cast microstructures: (a) A1, (b) A2, (c) A3, (d) A4.



**Figure 5.** X-ray diffraction patterns of the as-cast DS Fe–B alloys (i.e., longitudinal section).

### 3.2. The Static Oxidation Results

Figure 6 shows the weight gains per unit surface area for all DS samples at 1073 K. From Figure 6, it can be seen that the weight gains of  $\text{Fe}_2\text{B}_{//}$  samples increased with an increase in oxidation time. The weight gain of all alloys rapidly developed in the initial oxidation stage of 20 h, and subsequently began to slow down. Moreover, the oxidation weight gain per unit area displayed a decreasing trend with the increase in Si addition, and sample A4 showed a steady and slight oxidation behavior and also exhibited the lowest oxidation weight gain. Obviously, the addition of Si can promote the oxidation resistance of the  $\text{Fe}_2\text{B}_{//}$  samples of DS Fe–B alloy.

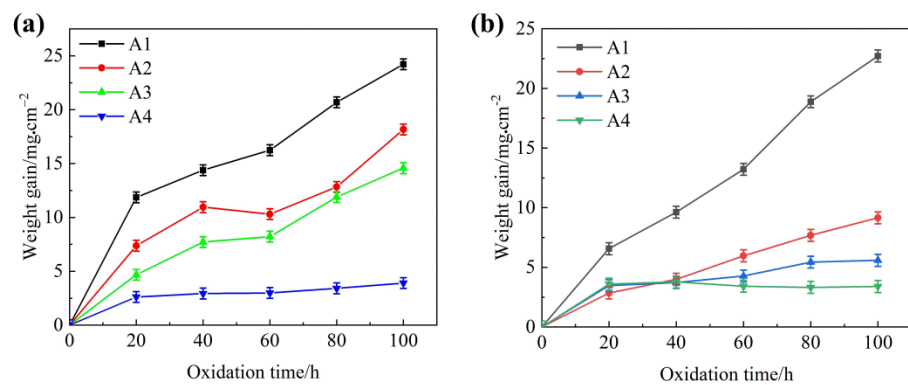


**Figure 6.** Weight gains per unit surface area as a function of oxidation time at 800 °C: (a) Fe<sub>2</sub>B<sub>//</sub> samples with various Si addition, (b) Fe<sub>2</sub>B<sub>⊥</sub> samples with various Si addition.

However, in the Fe<sub>2</sub>B<sub>⊥</sub> sample of the DS Fe–B alloy, the oxidation weight gains of A2, A3 and A4 of Fe<sub>2</sub>B<sub>⊥</sub> sample showed lower values than that of the Fe<sub>2</sub>B<sub>//</sub> samples except for sample A1. That is to say, with the increase in Si addition, the DS Fe–B alloy with Fe<sub>2</sub>B<sub>⊥</sub> sample possessed better oxidation resistance, which may be attributed to the Fe<sub>2</sub>B orientation effects, such as the Fe<sub>2</sub>B barrier layer and its oxidation resistance at different crystal orientations. Obviously, Si content in the matrix and Fe<sub>2</sub>B crystal orientation may have a synergistic role to demonstrate various oxidation resistances. When the oxidation time reached 40 h, the high-temperature oxidation weight gain curve of sample A4 with a Si addition of 3.50 wt.% displayed very slowly climbing behavior both in the Fe<sub>2</sub>B<sub>//</sub> and Fe<sub>2</sub>B<sub>⊥</sub> samples, which indicates that the increase in Si content has a strong oxidation inhibitory effect. It is worth noting that the static high-temperature oxidation resistance of the Fe<sub>2</sub>B<sub>⊥</sub> sample was significantly better than that of the Fe<sub>2</sub>B<sub>//</sub> sample, especially in the 1.50 wt.% Si and 2.50 wt.% Si samples (i.e., A2 and A3), but the A4 sample with 3.50 wt.% Si was approximately equal with the same values in the Fe<sub>2</sub>B<sub>//</sub> and Fe<sub>2</sub>B<sub>⊥</sub> samples. Undoubtedly, there is an obvious synergistic effect between Si addition and Fe<sub>2</sub>B crystal orientation.

The oxidation rate can be calculated using Equation (1) [40]:

$$K_p = \left( \frac{\Delta w}{A} \right)^2 t^{-1} \quad (1)$$

where  $K_p$  represents the oxidation rate ( $\text{mg}^2 \cdot \text{cm}^{-4} \cdot \text{s}^{-1}$ ),  $\Delta W$  is the weight gain (mg), and  $A$  and  $t$  are the surface area ( $\text{cm}^2$ ) of the samples and oxidation time (s), respectively. After sample A4 was oxidized for 100 h, the oxidation rate of the Fe<sub>2</sub>B<sub>⊥</sub> sample was  $0.115 \text{ mg}^2 \cdot \text{cm}^{-4} \cdot \text{s}^{-1}$ , which was better than that of the Fe<sub>2</sub>B<sub>//</sub> sample with an oxidation rate of  $0.152 \text{ mg}^2 \cdot \text{cm}^{-4} \cdot \text{s}^{-1}$ .

### 3.3. Surface Morphology of Oxide Scales

The Fe<sub>2</sub>B<sub>//</sub> oxidation surface morphologies of the oxide scales formed at 1073 K for 100 h are shown in Figure 7. It was observed that the oxide film on the surface of the DS Fe–B alloy without Si was relatively loose and rough with some holes and cracks, and more parts of the surface were cracked and wrinkled, which indicates that the oxide film was very easy to crack and peel off from the substrate (Figure 7a). From Figure 7b–d, with the increase in Si content, the oxide film of the DS Fe–B alloy became fairly compact, uniform and smooth. Furthermore, the emerging cracks and holes on the scales were gradually filled and vanished. Obviously, a large number of cracks and holes formed on the surface of sample A1 may provide fast channels for the diffusion of oxygen ions and thus promote the constant oxidation process [5]. With an increase in Si content, the inside of the oxide film became denser, preventing the outward diffusion of the internal matrix elements, and the surface became flatter. From Figure 8, the surface oxides of sample A1 were composed

of  $\text{Fe}_2\text{O}_3$ ,  $\text{M}_3\text{O}_4$  ( $\text{M} = \text{Fe}, \text{Cr}$ ) [41]. It is interesting to note that a small amount of  $\text{SiO}_2$  was obtained on the surface of the oxide film, which indicates that part of the Si may segregate at the substrate–scale interface and react with oxygen ions to form the inner  $\text{SiO}_2$  layer.

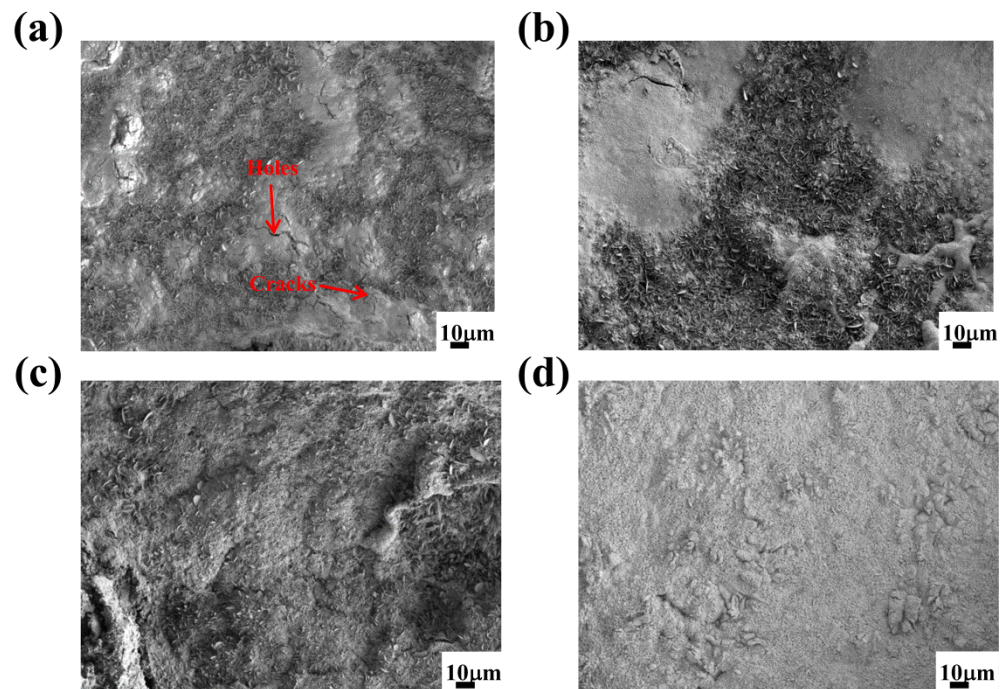


**Figure 7.** SEM micrographs of the  $\text{Fe}_2\text{B}_{//}$  sample surface of the scale formed by 100 h oxidation at 1073 K: (a) alloy A1, (b) alloy A2, (c) alloy A3, (d) alloy A4.

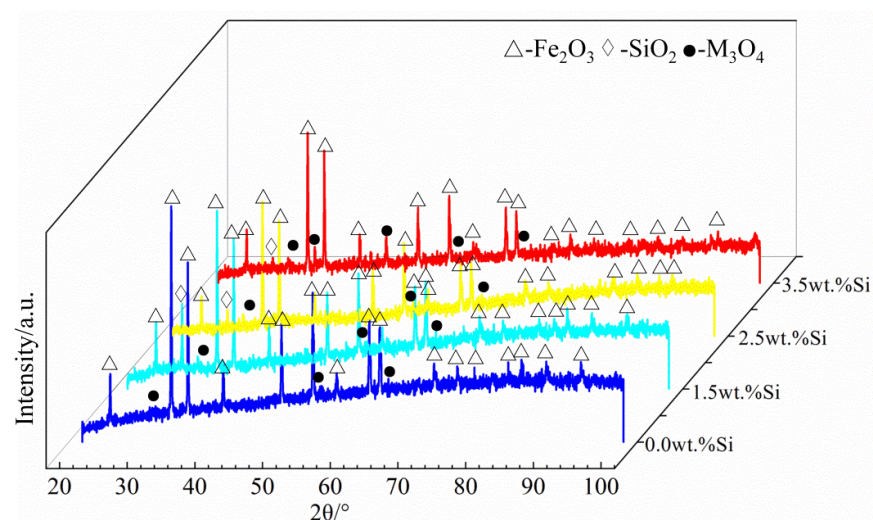
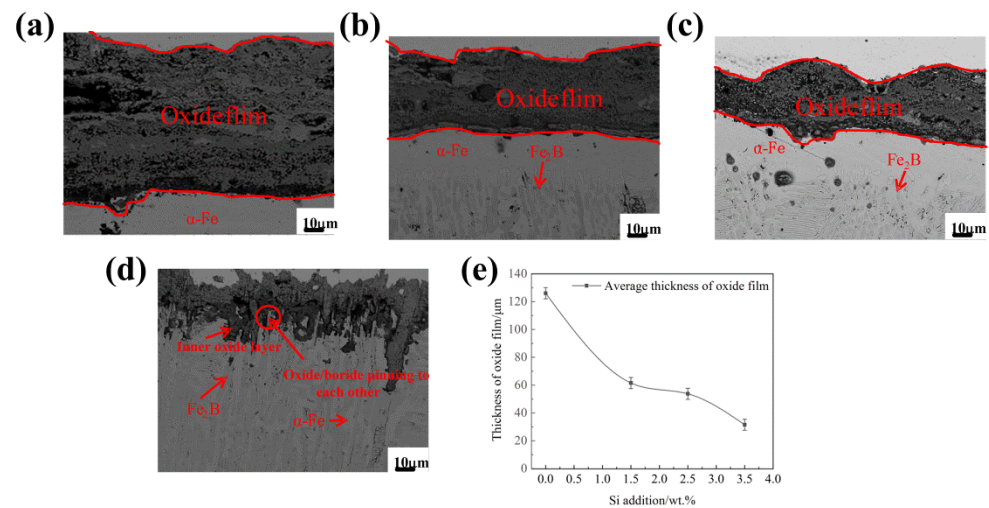


**Figure 8.** XRD on the surface of  $\text{Fe}_2\text{B}_{//}$  sample oxide film after oxidation for 100 h.

### 3.4. The Cross-Sectional Analysis of Oxide Scales

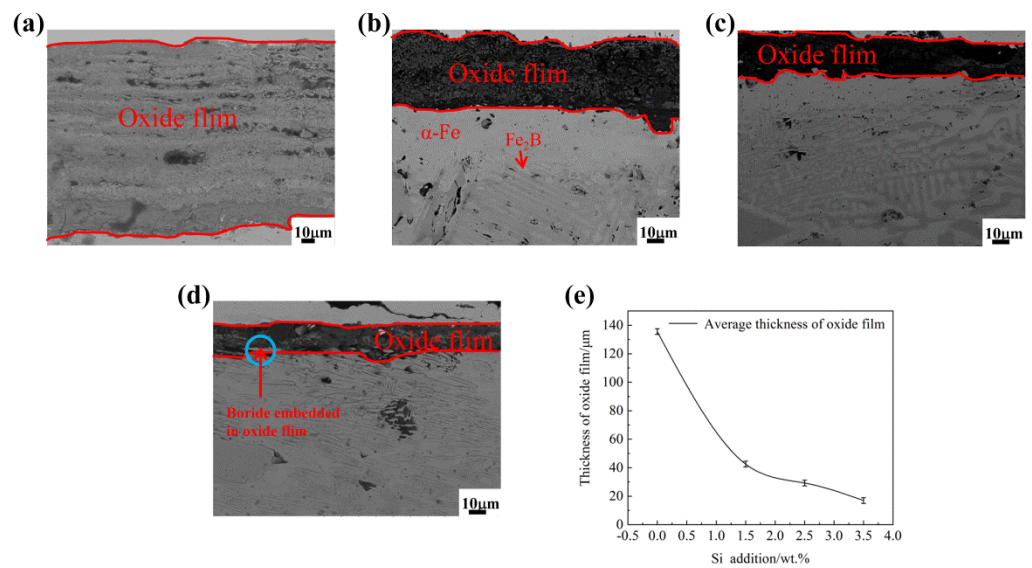
The cross-section morphologies for the  $\text{Fe}_2\text{B}_{//}$  samples oxidized for 60 h at 1073 K are shown in Figure 9. From Figure 9a, it can be seen that the oxide film of sample A1 without Si addition was thicker, and the average oxide film thickness reached 126.035  $\mu\text{m}$ . Furthermore, the overall oxide film was relatively porous and cracked, and there existed a large cleavage between the scales and substrate. Obviously, the combination of scale–substrate interface showed the internal bonding properties of the oxide films (e.g., cohesion of the scales, compactness of oxide film, etc.). However, when the Si content in the DS Fe–B alloy reached 1.50 wt.% and 2.50 wt.%, the thickness of the oxide film

gradually decreased, and the oxide film became compact and continuous, as shown in Figure 9b,c (e.g., A2 and A3 alloys). As shown in Figure 9d, the oxide film was arranged in a zigzag pattern at the scale–substrate interface, which was deeply embedded and planted into the columnar matrix and was well pinned with the boride to form a packaged structure of an inner SiO<sub>2</sub> film wrapped in columnar Fe<sub>2</sub>B grains. This means that oriented Fe<sub>2</sub>B at the inner interface can be pinned by internal growth SiO<sub>2</sub> to generate an interlocking interface between oriented Fe<sub>2</sub>B and internally grown SiO<sub>2</sub> so as to enhance the contact area of the scales and substrate as well as a pinning effect of the inner interface bulge or obstacle thus inhibiting the spallation of scales (as shown in Figure 9d for the A4 alloy). Clearly, the average thickness of cross-sectional oxide film decreased to 31.487 μm with the increase in Si content of 3.50 wt.%, as shown in Figure 9e. The A4 sample had the lowest oxidation rate of the Fe<sub>2</sub>B<sub>//</sub> samples. Thus, this implied that the higher the silicon content of the matrix, the better the oxidation resistance of the DS alloy with Fe<sub>2</sub>B<sub>//</sub> sample. There is no doubt that the addition of Si that forms an inner SiO<sub>2</sub> film hinders the inner diffusion of oxygen ions into the substrate and reduces the further growth and spallation of the oxide films, thus improving the high-temperature oxidation resistance of the DS alloy [31].



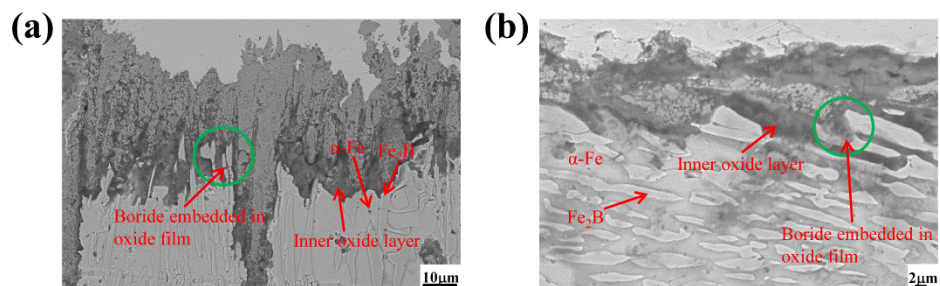
**Figure 9.** The BSE micrographs of the cross-section of Fe<sub>2</sub>B<sub>//</sub> samples oxidized for 60 h at 1073 K: (a) alloy A1, (b) alloy A2, (c) alloy A3, (d) alloy A4, (e) the thickness of cross-sectional oxide film.

Figure 10 shows the BSE micrographs of the cross-section of the Fe<sub>2</sub>B<sub>⊥</sub> samples oxidized for 60 h at 1073 K. It can be seen from Figure 10a, that the thickness of the oxide film for sample A1 without Si addition was larger than others. From Figure 10c,d, it can be seen that the oxide films of the A3 and A4 samples were relatively flat and uniform, while the boride [002] orientation and oxidation interface of the oxide film are distributed in parallel (i.e., Fe<sub>2</sub>B [002] orientation vertical to the oxidation direction). It is clear that in the A4 sample, with Fe<sub>2</sub>B [002] orientation vertical to the oxidation interface (i.e., Fe<sub>2</sub>B<sub>⊥</sub> sample with 3.50 wt.% Si addition), that some oxides formed by by-passing the boride with an emerging oxidation of the phase boundaries (i.e., α/Fe<sub>2</sub>B boundaries) appearing obliquely along the weak positions of the oriented Fe<sub>2</sub>B owing to the oxidation manner (i.e., Fe<sub>2</sub>B [002] orientation vertical to the oxidation direction) and probable Si segregation in these areas. By contrast, the average oxide film thickness of the Fe<sub>2</sub>B<sub>⊥</sub> samples was smaller than that of the Fe<sub>2</sub>B<sub>//</sub> samples, and the two oxidation manners of the Fe<sub>2</sub>B<sub>//</sub> and Fe<sub>2</sub>B<sub>⊥</sub> samples showed similar oxidation features with the increase in Si content in the DS Fe–B alloys (i.e., decrease in weight gains for both Fe<sub>2</sub>B<sub>//</sub> and Fe<sub>2</sub>B<sub>⊥</sub> samples with the increase in Si addition).



**Figure 10.** The BSE micrographs of the cross-section of Fe<sub>2</sub>B<sub>⊥</sub> samples oxidized for 60 h at 1073 K: (a) alloy A1, (b) alloy A2, (c) alloy A3, (d) alloy A4, (e) the thickness of cross-sectional oxide film.

Figure 11 shows the high-magnification SEM morphology of the Fe<sub>2</sub>B<sub>//</sub> and Fe<sub>2</sub>B<sub>⊥</sub> samples of the DS A4 alloy oxidized at 1073 K for 60 h. From Figure 11a, the oxide film in the Fe<sub>2</sub>B<sub>//</sub> sample was arranged in a zigzag pattern, and the internal oxidation was more serious owing to the insufficient synergy of oxidation between the matrix and oriented Fe<sub>2</sub>B in the DS Fe–B alloy despite more Si addition. However, the oriented boride and the oxide film were embedded into each other at their interfaces, which increased the bonding force and inhibited the spallation of scales. Meanwhile, it can be seen from Figure 11b that, the oriented boride was obliquely embedded into the oxide film and mainly played a barrier role in preventing the further oxidation and spallation of scales in the Fe<sub>2</sub>B<sub>⊥</sub> sample. Evidently, the Fe<sub>2</sub>B<sub>⊥</sub> sample dominated in oxidation resistance and possessed a better oxidation performance than the Fe<sub>2</sub>B<sub>//</sub> sample, which was attributed to the lack of synergy between the matrix and oriented Fe<sub>2</sub>B in the Fe<sub>2</sub>B<sub>//</sub> sample and the strong and beneficial barrier and inhibition of oxidation in the Fe<sub>2</sub>B<sub>⊥</sub> sample to hinder the diffusion of oxygen ions and spallation of scales [42].



**Figure 11.** High-magnification SEM morphology of the A4 sample oxidized for 60 h at 1073 K: (a) Fe<sub>2</sub>B<sub>//</sub> sample, (b) Fe<sub>2</sub>B<sub>⊥</sub> sample.

Figure 12 shows the cross-sectional line scanning analysis of the Fe<sub>2</sub>B<sub>//</sub> sample of the A4 alloy oxidized for 60 h at 1073 K. The thickness of the oxide film was about 35 μm. From Figures 8 and 12b, the oxide film was composed Fe<sub>2</sub>O<sub>3</sub>, Fe<sub>3</sub>O<sub>4</sub> and SiO<sub>2</sub> oxides. Fe<sub>2</sub>O<sub>3</sub> and Fe<sub>3</sub>O<sub>4</sub> mainly exist in the outer oxide layer, and an obvious internal oxidation is found at the boundary of substrate and oxide film (black zone at the bottom of the oxide film), it can be found that the inner oxide layer is a SiO<sub>2</sub> layer. This SiO<sub>2</sub> oxide scale is not only

compact and continuous, but also presents strong and perfect adhesion to the metallic substrate [31,33], which may well hinder further  $O^{2-}$  diffusion into the matrix [31,33].

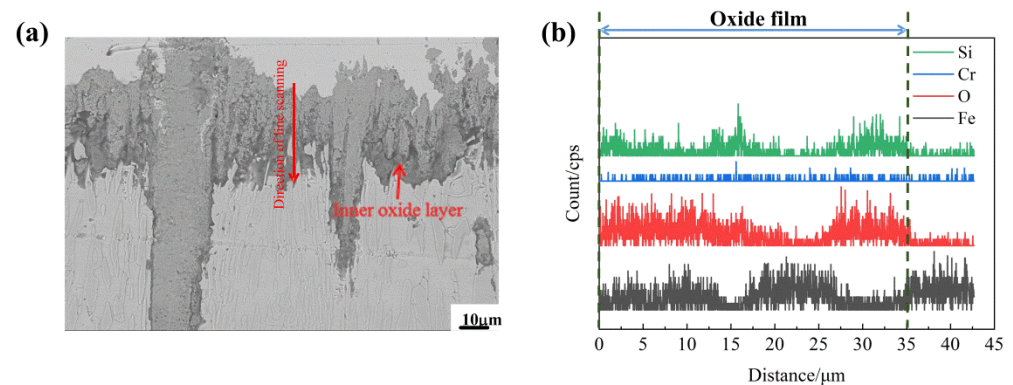


**Figure 12.** Line scanning analysis of a cross-section of the  $Fe_2B_{//}$  A4 sample oxidized for 60 h at 1073 K: (a) diagram of line scan, (b) curve change diagram of each element of the line scan.

Figure 13 shows the EDS mapping of a cross-section of the  $Fe_2B_{\perp}$  sample in the A4 alloy oxidized for 60 h at 1073 K. It is clear that the O element was uniformly distributed in the whole oxide film. However, due to the small diffusion coefficient of Si, it was concentrated in the lower part of the oxide film to form a thin layer of  $SiO_2$ , particularly at the inner interface, which infers that the internal oxidation of the  $Si^{+4}$  cation occurs at the inner interface [5,43]. Si was sparsely distributed in the upper part of the oxide film, while Fe was distributed in the whole oxide film and can react with  $O^{2-}$  ions to form  $Fe_2O_3$  and  $Fe_3O_4$ . Compared with the  $Fe_2B_{//}$  oriented sample, Si in the  $Fe_2B_{\perp}$  oriented sample was more concentrated and enriched at the bottom of the oxide film.

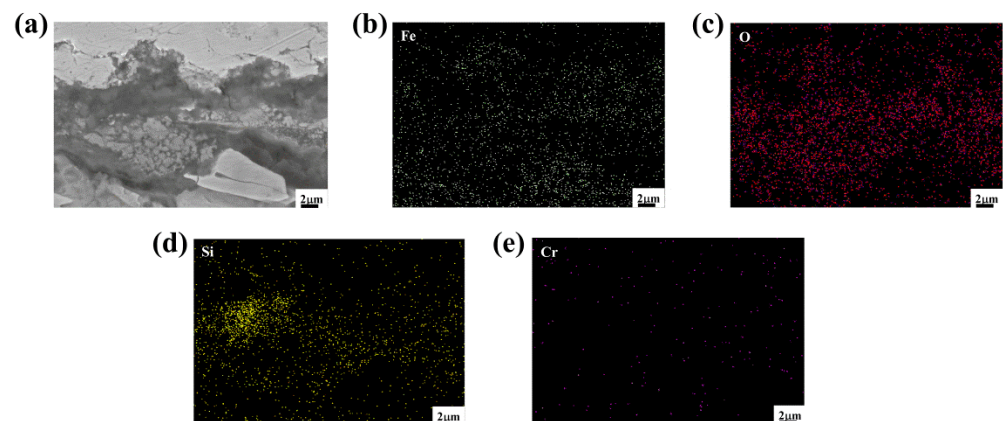


**Figure 13.** The EDS mapping of a cross-section of the  $Fe_2B_{\perp}$  A4 sample oxidized for 60 h at 1073 K: (a) micrograph of surface scanning, (b) element distribution of Fe, (c) element distribution of O, (d) element distribution of Si, (e) element distribution of Cr.

### 3.5. Mechanism of High-Temperature Oxidation Resistance of Directionally Solidified Fe–B Alloys with Different Orientations

According to the oxidation rate, the oxidation characteristics of DS Fe–B alloys are sensitive to the Si content and boride orientation. The oxidation results indicate that scale grows by a diffusion-controlled process. Since the diffusion coefficient of Si is much smaller than that of Fe, Si will tend to produce an internal oxide layer at the interface between the oxide film and the substrate [43,44]. The schematic diagram of the high-temperature oxidation resistance mechanism of DS Fe–B alloys with different boride orientations and Si content is shown in Figure 14. From Figure 14a, in the  $Fe_2B_{//}$  sample, the  $Fe_2B$  hard-phase in the matrix grew in a directional columnar arrangement and was embedded in the

oxide film, and the upper part of the oxide film was mainly composed of  $\text{Fe}_2\text{O}_3$  and  $\text{Fe}_3\text{O}_4$ . However, due to the voids and cracks in the oxide film, the metal cations could easily diffuse out and partly distribute into the oxide film during the oxidation. Additionally, voids and cracks could be used as a channel allowing  $\text{O}^{2-}$  ions to rapidly enter into the matrix of the DS alloy through this channel to form scales [23]. Since the free energy of Si oxide is lower than that of Fe oxide, it can be preferentially oxidized, and the inwardly diffused  $\text{O}^{2-}$  and  $\text{Si}^{4+}$  can form a significant  $\text{SiO}_2$  inner oxide layer [43–45]. The inwardly protruding  $\text{SiO}_2$  thin layer and the oriented  $\text{Fe}_2\text{B}$  embedded into the oxide film pin each other increasing the bonding force of the scales, which can improve the anti-peeling performance of the oxide film. The formed  $\text{SiO}_2$  thin layer can further impede the inward diffusion of  $\text{O}^{2-}$  and improve the high-temperature oxidation resistance of the DS alloy [31].

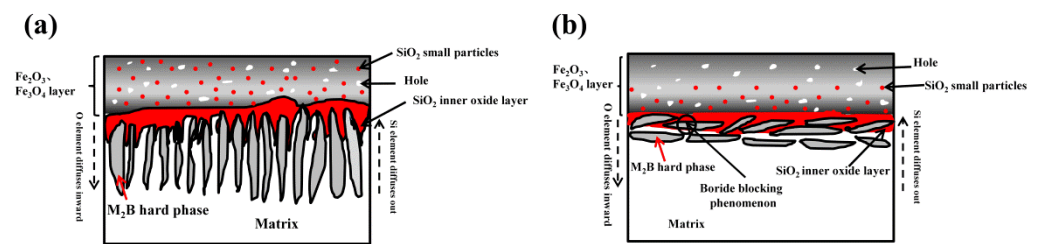


**Figure 14.** Schematic diagrams of high-temperature oxidation mechanisms: (a)  $\text{Fe}_2\text{B}_{//}$  A4 sample, (b)  $\text{Fe}_2\text{B}_{\perp}$  A4 sample.

Different from Figure 14b, in the  $\text{Fe}_2\text{B}_{\perp}$  sample the  $\text{Fe}_2\text{B}$  [002] orientation was parallel to the oxidation direction and was partly embedded into the oxide film obliquely. Due to the blocking effect of borides,  $\text{Si}^{4+}$  cannot continue to diffuse outward through the inner interface and is mainly concentrated and enriched at the bottom of the oxide film to form a  $\text{SiO}_2$  oxide layer, which depends on the  $\text{O}^{2-}$  inner-diffusion controlled process. Therefore, the overall anti-oxidation performance of the  $\text{Fe}_2\text{B}_{\perp}$  sample was better than that of the  $\text{Fe}_2\text{B}_{//}$  sample owing to the combined effects of Si content and  $\text{Fe}_2\text{B}$  orientation.

#### 4. Conclusions

In this work, the as-cast DS Fe–B alloys with various Si contents and different boride orientations were designed and fabricated, and their as-cast microstructures and static oxidation behaviors were investigated extensively. The main conclusions can be summarized as follows:

- (1) The as-cast DS Fe–B alloys consist of columnar  $\text{Fe}_2\text{B}$  and  $\alpha\text{-Fe}$ . The Si-containing microstructures of the DS Fe–B alloys show good orientation effects. The columnar gray  $\text{Fe}_2\text{B}$  borides are arranged in long rods with  $\text{Fe}_2\text{B}$  [002] crystal orientations as the preferred growth direction, and the gray-white  $\alpha\text{-Fe}$  matrix is distributed among the laminated structure of  $\text{Fe}_2\text{B}$  grains to display a dual-phase oriented microstructures of the DS Fe–B alloys.
- (2) When the preferred growth direction of  $\text{Fe}_2\text{B}$  [002] orientation is parallel to the oxidation direction (marked as  $\text{Fe}_2\text{B}_{//}$  sample), the oxidation weight gain decreases with the increase in Si content, and reaches the lowest value at 3.50 wt.% Si addition, which is attributed to the presence of a certain amount of an internal  $\text{SiO}_2$  film with obvious sawtooth-shaped structure except for outermost layer of  $\text{Fe}_2\text{O}_3$ ,  $\text{M}_3\text{O}_4$  ( $M = \text{Fe}, \text{Cr}$ ) scales, which is embedded into the matrix and exhibits a beneficial role to improve the anti-peeling performance of the oxide film.
- (3) In the high-temperature static oxide film of the  $\text{Fe}_2\text{B}_{\perp}$  sample (i.e.,  $\text{Fe}_2\text{B}$  [002] orientation perpendicular to the oxidation direction), Si is mainly concentrated and enriched in the lower part of the oxide film to form a  $\text{SiO}_2$  thin layer. The Si-rich internal oxidation layer and the blocking effect of oriented boride can effectively hinder further

internal diffusion of oxygen ions and improve the anti-oxidation performance, which shows better oxidation resistance than that of the Fe<sub>2</sub>B// sample.

**Author Contributions:** Conceptualization and writing, P.G., L.X. and S.M.; Methodology and testing, P.G., P.L., J.J. and X.H.; Sample preparation and testing, P.G., Y.L. and P.L.; Microstructure analysis and editing, P.G., Y.L. and X.C.; Writing and Analysis—original draft preparation, P.G. and S.M.; Writing—review and editing, P.G., S.M. and J.X.; Supervision, conceptualization and analysis, S.M. All authors have read and agreed to the published version of the manuscript.

**Funding:** This research was funded by the funds of the National Natural Science Foundation of China with grant numbers 52071254, 52271069 and 51771143, and the National Joint Engineering Research Center for abrasion control and molding of metal materials with grant number HKDNM201801, and the Foundational Research Funds for the Central Universities with Grant No. xzy012020002.

**Institutional Review Board Statement:** Not applicable.

**Informed Consent Statement:** Not applicable.

**Data Availability Statement:** Data sharing is not applicable to this article.

**Conflicts of Interest:** The authors declare no conflict of interest.

## References

1. Balloy, D.; Tissier, J.C.; Giorgi, M.; Briant, M. Corrosion mechanisms of steel and cast iron by molten aluminum. *Metall. Mater. Trans. A* **2010**, *41*, 2366–2376. [[CrossRef](#)]
2. Zhang, X.M.; Chen, W.P. Review on corrosion-wear resistance performance of materials in molten aluminum and its alloys. *Trans. Nonferrous Met. Soc. China* **2015**, *25*, 1715–1731. [[CrossRef](#)]
3. Xu, G.P.; Wang, K.; Dong, X.P.; Jiang, H.Y.; Wang, Q.D.; Ye, B.; Ding, W.J. Multiscale corrosion-resistance mechanisms of novel ferrous alloys in dynamic aluminum melts. *Corros. Sci.* **2020**, *163*, 108276. [[CrossRef](#)]
4. Ling, Z.C.; Chen, W.P.; Lu, T.W.; Li, B.; Zhang, X.M. Interfacial morphology and tribo-corrosion behaviour of Fe-15.3 wt% Cr-3.1 wt% B-6.2 wt% Mo alloy in molten aluminium. *Wear* **2019**, *430*, 81–93. [[CrossRef](#)]
5. Xu, G.P.; Wang, K.; Li, H.N.; Ju, J.; Dong, X.P.; Jiang, H.Y.; Wang, Q.D.; Ding, W.J. In situ nanoparticle-induced anti-oxidation mechanisms: Application to FeCrB alloys. *Corros. Sci.* **2021**, *190*, 109656. [[CrossRef](#)]
6. Ma, S.Q.; Xing, J.D.; Yi, D.W.; Fu, H.G.; Liu, G.F.; Ma, S.C. Microstructure and corrosion behavior of cast Fe-B alloys dipped into liquid zinc bath. *Mater. Charact.* **2010**, *61*, 866–872. [[CrossRef](#)]
7. Ma, S.Q.; Xing, J.D.; He, Y.L.; Fu, H.G.; Li, Y.F.; Liu, G.Z. Effect of orientation and lamellar spacing of Fe<sub>2</sub>B on interfaces and corrosion behavior of Fe-B alloy in hot-dip galvanization. *Acta Mater.* **2016**, *115*, 392–402. [[CrossRef](#)]
8. Wang, Y.; Xing, J.D.; Fu, H.G.; Liu, Y.Z.; Zheng, K.H.; Ma, S.Q.; Jian, Y.X. Interfacial morphology and corrosion-wear behavior of cast Fe-3.5 wt.% B steel in liquid zinc. *Corros. Sci.* **2018**, *131*, 290–299. [[CrossRef](#)]
9. Zhang, X.M.; Chen, W.P.; Luo, H.F.; Li, S.; Zhou, T.; Shi, L.Y. Corrosion resistance and interfacial morphologies of novel Fe-Cr-Mo-B cast steels in molten aluminum. *Corros. Sci.* **2017**, *125*, 20–28. [[CrossRef](#)]
10. Wang, M.M.; Xue, J.; Gao, R.; Gao, H.Y.; Zhou, Y.; Zhao, Y.Y.; Liu, Y.H.; Kang, M.D.; Wang, J. Interface morphology and corrosion behavior of bulk Fe<sub>2</sub>B in liquid Al. *Mater. Charact.* **2019**, *152*, 1–11. [[CrossRef](#)]
11. Li, F.; Li, Z. Study on improvement of hard phase morphology and properties of hypoeutectic Fe-C-B alloy. *J. Alloys Compd.* **2014**, *587*, 267–272. [[CrossRef](#)]
12. Yi, Y.L.; Li, Q.; Long, S.L.; Lv, Z.; Li, S.J.; Liu, Y.Z.; Zheng, B.C.; Li, W. Effect of matrix microstructure on the matrix/M<sub>2</sub>B wear interaction and its quantitative characterization in an Fe-2wt%B alloy. *Wear* **2021**, *472–473*, 203608. [[CrossRef](#)]
13. Ren, X.Y.; Fu, H.G.; Xing, J.D.; Yi, Y.L. Effect of solidification rate on microstructure and toughness of Ca-Ti modified high boron high speed steel. *Mater. Sci. Eng. A* **2019**, *742*, 617–627. [[CrossRef](#)]
14. Yang, Y.W.; Fu, H.G.; Wang, K.M.; Zhu, L.L.; Jang, L. Thermodynamic calculation and analysis for aluminum-alloyed high boron high speed steel. *Mater. Werkst.* **2018**, *49*, 39–53. [[CrossRef](#)]
15. Yuan, Z.T.; Jiang, Y.H.; Li, L.; Li, Z.L. The microstructure and high-temperature tribology behavior of high boron HSS under different heat treatments. *Ind. Lubr. Tribol.* **2019**, *71*, 212–220. [[CrossRef](#)]
16. Cen, Q.; Fu, H. A study of heat treatment of high-boron high-speed steel roll. *Mater. Werkst.* **2013**, *44*, 612–617. [[CrossRef](#)]
17. Qihong, C.; Zhan-Wen, W.; Yi, J.; Yehua, J.; Fei, L.; Hanguang, F. A study of centrifugal cast high boron high speed steel. *Mater. Werkst.* **2014**, *45*, 582–590. [[CrossRef](#)]
18. Yan, P.X.; Zhang, X.M.; Xu, J.W.; Wu, Z.G.; Song, Q.M. High-temperature behavior of the boride layer of 45# carbon steel. *Mater. Chem. Phys.* **2001**, *71*, 107–110.
19. Kim, J.H.; Hong, H.S.; Kim, S.J. Effect of boron addition on the cavitation erosion resistance of Fe-based hardfacing alloy. *Mater. Lett.* **2007**, *61*, 1235–1237. [[CrossRef](#)]

20. Klein, L.; Bauer, A.; Neumeier, S.; Virtanen, S. High temperature oxidation of  $\gamma/\gamma'$ -strengthened Co-base superalloys. *Corros. Sci.* **2011**, *53*, 2027–2034. [[CrossRef](#)]
21. Wu, J.Y.; Wang, W.; Zhou, C.G. Microstructure and oxidation resistance of Mo–Si–B coating on Nb based in situ composites. *Corros. Sci.* **2014**, *87*, 421–426. [[CrossRef](#)]
22. Zhong, D.H.; Sano, H.; Uchiyama, Y.; Kobayashi, K. Effect of low-level boron doping on oxidation behavior of polyimide-derived carbon films. *Carbon* **2000**, *38*, 1199–1206. [[CrossRef](#)]
23. Perez-Enciso, E.; Ramos, M.A.; Vieira, S. Low-temperature specific heat of different B<sub>2</sub>O<sub>3</sub> glasses. *Phys. Rev. B* **1997**, *56*, 32. [[CrossRef](#)]
24. Moon, O.M.; Kang, B.C.; Lee, S.B.; Boo, J.H. Temperature effect on structural properties of boron oxide thin films deposited by MOCVD method. *Thin Solid Films* **2004**, *464*, 164–169. [[CrossRef](#)]
25. Churyumov, A.V.; Pozdniakov, A.V.; Mondoloni, B.; Prosviryakov, A.S. Effect of boron concentration on hot deformation behavior of stainless steel. *Res. Phys.* **2019**, *13*, 102340. [[CrossRef](#)]
26. Pan, F.S.; Hirohashi, M.; Lu, Y.; Ding, P.D.; Tang, A.T.; Edmonds, D.V. Carbides in high-speed steels containing silicon. *Metall. Mater. Trans. A-Phys. Metall. Mater. Sci.* **2004**, *35A*, 2757–2766. [[CrossRef](#)]
27. Cai, M.H.; Ding, H.; Zhang, J.S.; Li, L.; Li, X.B.; Du, L.X. Transformation Behavior of Low Carbon Steels Containing Two Different Si Contents. *J. Iron Steel Res. Int.* **2009**, *16*, 55–60. [[CrossRef](#)]
28. Bhadeshia, H.K.D.H.; Edmonds, D.V. Analysis of mechanical properties and microstructure of high-silicon dual-phase steel. *Met. Sci.* **1980**, *14*, 41–49. [[CrossRef](#)]
29. Setia, P.; Venkateswaran, T.; Tharian, K.T.; Jain, J.; Singh, S.S.; Shekhar, S. Influence of Si content on the microstructure and mechanical properties of silicon stainless steel. *Mater. Sci. Eng. A* **2022**, *829*, 142141. [[CrossRef](#)]
30. Ju, J.; Yang, C.; Ma, S.Q.; Kang, M.D.; Wang, K.M.; Li, J.J.; Fu, H.G.; Wang, J. Effect of temperature on oxidation resistance and isothermal oxidation mechanism of novel wear-resistant Fe–Cr–B–Al–C–Mn–Si alloy. *Corros. Sci.* **2020**, *170*, 108620. [[CrossRef](#)]
31. Esleben, K.; Gorra, B.; Christa, H.J.; Mukherjib, D.; Rösleret, J. The effect of Ni and Si additions on the oxidation behaviour of Co-17Re-18Cr alloys. *Corros. Sci.* **2019**, *159*, 108135. [[CrossRef](#)]
32. Lv, Z.; Fu, H.G.; Xing, J.D.; Huang, Z.F.; Ma, S.Q.; Hu, Y. Influence of boron contents on oxidation behavior and the diffusion mechanism of Fe–B based alloys at 1073K in air. *Corros. Sci.* **2016**, *108*, 185–193. [[CrossRef](#)]
33. Zhang, P.; Li, Y.T.; Chen, Z.; Zhang, J.Y.; Shen, B.L. Oxidation response of a vacuum arc melted NbZrTiCrAl refractory high entropy alloy at 800–1200 °C. *Vacuum* **2019**, *162*, 20–27. [[CrossRef](#)]
34. Guo, P.J.; Ma, S.Q.; He, X.B.; Shah, I.A.; Lv, P.; Chen, H.T.; Xing, J.D.; Xu, L.J.; Zhang, J.K. Effect of Silicon Content on Microstructures and Properties of Directionally Solidified Fe–B Alloy. *Materials* **2022**, *15*, 5937. [[CrossRef](#)] [[PubMed](#)]
35. Yan, J.B.; Gao, Y.M.; Liang, L.; Ye, Z.Z.; Li, Y.F.; Chen, W.; Zhang, J.J. Effect of yttrium on the cyclic oxidation behaviour of HP40 heat-resistant steel at 1373K. *Corros. Sci.* **2011**, *53*, 329–337. [[CrossRef](#)]
36. Liu, Z.; Li, Y.; Chen, X.; Hu, K. Microstructure and mechanical properties of high boron white cast iron. *Mater. Sci. Eng. A* **2008**, *486*, 112–116. [[CrossRef](#)]
37. Lv, Z.; Fu, H.G.; Xing, J.D.; Ma, S.Q.; Hu, Y. Microstructure and crystallography of borides and mechanical properties of Fe–B–C–Cr–Al alloys. *J. Alloys Compd.* **2016**, *662*, 54–62. [[CrossRef](#)]
38. Guo, C.Q.; Kelly, P.M. Boron solubility in Fe–Cr–B cast irons. *Mater. Sci. Eng. A* **2003**, *352*, 40–45. [[CrossRef](#)]
39. Wang, Y.; Xing, J.D.; Ma, S.Q.; Zheng, B.C.; Liu, G.Z.; Yang, D.X.; Bai, Y.P. Interface characterization and erosion–corrosion behavior of directional Fe-3.5 wt.% B steel in flowing liquid zinc at various temperatures. *Corros. Sci.* **2016**, *104*, 260–268. [[CrossRef](#)]
40. Weller, K.; Wang, Z.M.; Jeurgens, L.P.H.; Mittemeijer, E.J. Oxidation kinetics of amorphous Al<sub>x</sub>Zr<sub>1-x</sub> alloys. *Acta Mater.* **2016**, *103*, 311–321. [[CrossRef](#)]
41. Guo, P.J.; Ma, S.Q.; Jiao, M.; Lv, P.; Xing, J.D.; Xu, L.J.; Huang, Z.F. Effect of chromium on microstructure and oxidation wear behavior of high-boron high-speed steel at elevated temperatures. *Materials* **2022**, *15*, 557. [[CrossRef](#)] [[PubMed](#)]
42. Wang, Y.; Xing, J.D.; Ma, S.Q.; Liu, G.Z.; He, Y.L.; Yang, D.X.; Bai, Y.P. Effect of Fe<sub>2</sub>B orientation on erosion–corrosion behavior of Fe–3.5 wt.% B steel in flowing zinc. *Corros. Sci.* **2016**, *98*, 240–248. [[CrossRef](#)]
43. Wang, J.; Lu, S.P.; Rong, L.J.; Li, D.Z.; Li, Y.Y. Effect of silicon on the oxidation resistance of 9 wt.% Cr heat resistance steels in 550 °C lead-bismuth eutectic. *Corros. Sci.* **2016**, *111*, 13–25. [[CrossRef](#)]
44. Bowen, A.W.; Leak, G.M. Diffusion in Bcc iron base alloys. *Metall. Trans.* **1970**, *1*, 2767–2773. [[CrossRef](#)]
45. Ju, J.; Kang, M.D.; Wang, K.M.; Zhou, Y.; Jiang, M.; Zhao, Y.Y.; Zhang, Z.; Wang, J.; Fu, H.G. Studies on as-cast microstructure and oxidation behavior of the Fe–Cr–B–Al alloys at 1073 K. *Vacuum* **2019**, *164*, 436–448. [[CrossRef](#)]